

Color Fourier single-pixel imaging with random color filter array

Jialiang Chen(陈佳亮), Wei Zhu(朱维), Le Wang(王乐), and Shengmei Zhao(赵生妹)
Citation: Chin. Phys. B, 2025, 34 (**9**): 094210. DOI: 10.1088/1674-1056/adf1e9
http://cpb.iphy.ac.cn; http://iopscience.iop.org/cpb

What follows is a list of articles you may be interested in

Computational temporal ghost imaging based on complementary modulation

Jia-Wei Li(李佳炜), Wei Zhang(张伟), Xue-Feng Liu(刘雪峰), and Xu-Ri Yao(姚旭日)
Chin. Phys. B, 2024, 33 (**11**): 114201. DOI: 10.1088/1674-1056/ad74e8

Image encryption algorithm based on multiple chaotic systems and improved Joseph block scrambling

Dingkang Mou(牟定康) and Yumin Dong(董玉民)
Chin. Phys. B, 2024, 33 (**10**): 104205. DOI: 10.1088/1674-1056/ad6257

High-quality ghost imaging based on undersampled natural-order Hadamard source

Kang Liu(刘炕), Cheng Zhou(周成), Jipeng Huang(黄继鹏), Hongwu Qin(秦宏伍), Xuan Liu(刘轩), Xinwei Li(李鑫伟), and Lijun Song(宋立军)
Chin. Phys. B, 2024, 33 (**9**): 094204. DOI: 10.1088/1674-1056/ad62e1

Complex-amplitude Fourier single-pixel imaging via coherent structured illumination

Hong-Yun Hou(侯红云), Ya-Nan Zhao(赵亚楠), Jia-Cheng Han(韩佳成), De-Zhong Cao(曹 德忠),Su-Heng Zhang(张素恒), Hong-Chao Liu(刘宏超), and Bao-Lai Liang(梁宝来)
Chin. Phys. B, 2023, 32 (**6**): 064201. DOI: 10.1088/1674-1056/ac8e9a

Fast Fourier single-pixel imaging based on Sierra-Lite dithering algorithm

Zhen-Yu Liang(梁振宇), Zheng-Dong Cheng(程正东), Yan-Yan Liu(刘严严), Kuai-Kuai Yu(于快快), Yang-Di Hu(胡洋頔)
Chin. Phys. B, 2019, 28 (**6**): 064202. DOI: 10.1088/1674-1056/28/6/064202

Color Fourier single-pixel imaging with random color filter array

Jialiang Chen(陈佳亮), Wei Zhu(朱维), Le Wang(王乐)†, and Shengmei Zhao(赵生妹)

School of Communications and Information Engineering, Nanjing University of Posts and Telecommunications, Nanjing 210003, *China*

(Received 22 March 2025; revised manuscript received 13 July 2025; accepted manuscript online 19 July 2025)

Color Fourier single-pixel imaging (FSI) enables efficient spectral and spatial imaging. Here, we propose a Fourier single-pixel imaging scheme with a random color filter array (FSI-RCFA). The proposed method employs a random color filter array (RCFA) to modulate Fourier patterns. A three-step phase-shifting technique reconstructs the Fourier spectrum, followed by an RCFA-based demosaicing algorithm to recover color images. Compared to traditional color FSI based on Bayer color filter array schemes (FSI-BCFA), our approach achieves superior separation between chrominance and luminance components in the frequency domain. Simulation results demonstrate that the FSI-RCFA method achieves a lower mean squared error (MSE), a higher peak signal-to-noise ratio (PSNR), and superior noise resistance compared to FSI-BCFA, while enabling direct single-channel pixel measurements for targeted applications such as agricultural defect detection.

Keywords: color single-pixel imaging, Fourier single-pixel imaging, random color filter array, demosaicing algorithm, noise resistance

PACS: 42.30.Va, 42.30.Wb

DOI: 10.1088/1674-1056/adf1e9 **CSTR:** 32038.14.CPB.adf1e9

1. Introduction

Single-pixel imaging technique,[1–4] as an emerging imaging method, has received extensive attention and research in recent years. It can be traced back to Paul Nipkow,[5] who proposed a 'flying spot' camera that achieved spatial point sampling through mechanical scanning, laying the physical foundation for single-pixel imaging. In 1995, Pittman *et al.*[6] experimentally demonstrated ghost imaging for the first time using entangled photon pairs, reconstructing object images based on the correlation properties of biphotons. In 2002, Bennink *et al.*[7] showed the feasibility of ghost imaging without quantum entanglement by employing a classical thermal light source and random speckle modulation. Their method achieved image reconstruction based on statistical correlations in the intensity fluctuations of the light field. In 2009, Katz *et al.*[8] incorporated compressed sensing into single-pixel imaging, enabling undersampled reconstruction by exploiting sparsity. In the early 2010s, breakthroughs were made in orthogonal basis imaging, primarily using Hadamard[9] and Fourier bases.[10] In 2015, Zhang *et al.*[11] proposed Fourier single-pixel imaging (FPSI), which involves the modulation of the illumination or detection light field using Fourier patterns, followed by intensity measurement and image reconstruction via inverse Fourier transform. In addition, FPSI can also be applied to various fields, such as moiré encryption[12] and information transmission.[13] Compared with traditional imaging techniques, single-pixel imaging can not only realize high-quality and high-efficiency imaging,[14–16] but also meet the challenges of imaging in non-visible light bands, which further expands the range of applications of imaging techniques.

Color images not only contain spatial information about objects but also rich spectral information; therefore, it is of great significance to develop color imaging in the visible band. For color single-pixel imaging, two approaches have been proposed: on the one hand, time-sharing imaging and filter switching based on the principle of time-division multiplexing;[17–21] on the other hand, a split-optical-path structure with parallel detection, corresponding to space-division multiplexing.[22–24] In addition, some studies have proposed color Fourier single-pixel imaging based on the principle of two-dimensional discrete Fourier transform (DFT) for color imaging based on methods such as frequency division multiplexing[25–28] and compression-aware optimization.[4,29] Moreover, in 2018, Zhang *et al.*[30] multiplied a Bayer color filter array (BCFA)[31] with Fourier patterns to obtain color patterns and interacted with the object, which enabled color image reconstruction at a much lower hardware cost.

In color image processing, image information is commonly decomposed into luminance and chrominance components. Luminance represents the brightness characteristics of the scene, while chrominance describes color differences. However, periodic color filter arrays (CFAs), such as the BCFA, can lead to artifacts and interference[12] due to the overlap of chrominance components with luminance components in the frequency domain. To address this issue, Laurent Condat[32] proposed the random color filter array (RCFA), which is nonperiodic. It makes the colors of adjacent pixels different and concentrates chrominance energy in high-

†Corresponding author. E-mail: njwanglele@163.com

© 2025 Chinese Physical Society and IOP Publishing Ltd. All rights, including for text and data mining, AI training, and similar technologies, are reserved.

frequency regions. This conversion of aliasing into incoherent noise significantly reduces visually perceptible structural artifacts.

In this paper, we propose a Fourier single-pixel imaging scheme with a random color filter array (FSI-RCFA). Initially, we introduce the design method of the color Fourier pattern, which emerges through the modulation of the Fourier pattern by the RCFA. The RCFA is generated utilizing the RCFA generation algorithm. Subsequently, we employ Fourier single-pixel imaging with RCFA to accomplish the reconstruction of grayscale images. Finally, we propose the RCFA-based demosaicing algorithm to produce color images.[33]

Our proposed scheme has several advantages: first, it demonstrates high imaging quality, with smaller mean squared error (MSE) and higher peak signal-to-noise ratio (PSNR) metrics. Compared to single-pixel imaging schemes based on BCFA, our scheme significantly enhances imaging quality, particularly in terms of higher fidelity in image detail restoration. Second, our system exhibits superior noise resistance, effectively mitigating both internal and external noise. Third, our scheme is better suited to meet the requirements of specific scenarios, such as obtaining accurate single-channel pixel values at specific locations within the image.

2. FSI-RCFA

The FSI-RCFA is shown in Fig. 1.

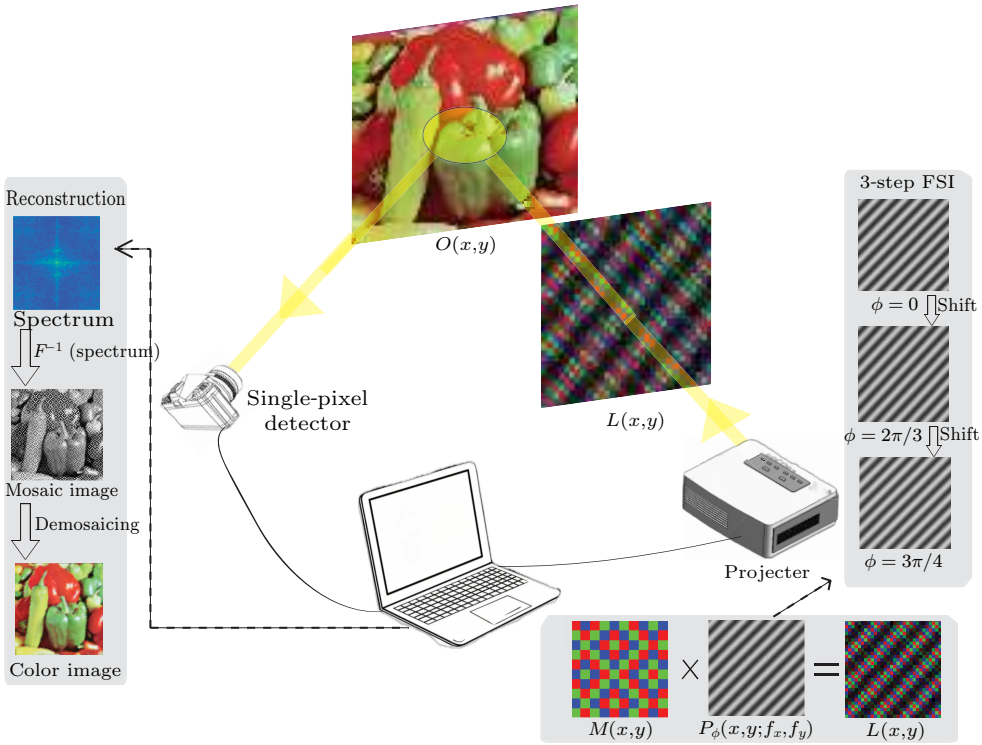


Fig. 1. Schematic diagram of color Fourier single pixel imaging based on an RCFA.

First, we present the design of the color Fourier pattern used for illumination. The RCFA modulates the Fourier pattern to generate the color Fourier pattern

$$L_\phi(x,y;f_x,f_y) = M(x,y) \times P_\phi(x,y;f_x,f_y), \tag{1}$$

where $M(x,y)$ refers to the RCFA, and $P_\phi(x,y;f_x,f_y)$ refers to a Fourier pattern with a two-dimensional sinusoidal structure, which can be written as

$$P_\phi(x,y;f_x,f_y) = a + b\cos\left(2\pi f_x x + 2\pi f_x x + \phi\right), \tag{2}$$

where a is the average intensity, b is the contrast, f_x and f_y are the spatial frequencies corresponding to the x and y directions, respectively, and ϕ is the initial phase ($\phi = 0, 2\pi/3$, and $4\pi/3$).

We now use the RCFA generation algorithm to form $M(x,y)$. It is possible to generate an RCFA of any size using this algorithm, but here we only describe the generation of the 6×6 array shown in Fig. 2. The RCFA is generated by the following three steps.

Step 1 Generate the first row. We store the six arrangement cases of red, green, and blue (RGB) colors in the matrix $\boldsymbol{A}$,

$$\boldsymbol{A} = \begin{bmatrix} \text{RGB} \\ \text{RBG} \\ \text{GRB} \\ \text{GBR} \\ \text{BRG} \\ \text{BGR} \end{bmatrix}, \tag{3}$$

where $\boldsymbol{A}$ is a matrix of size 6×3. Here, R stands for red, G

stands for green, and B stands for blue. To correctly generate the RCFA, we also need the adjacency rules, which we store in the matrix $\boldsymbol{B}$,

$$\boldsymbol{B} = \begin{bmatrix} 2 & 3 \\ 1 & 5 \\ 1 & 4 \\ 3 & 6 \\ 2 & 6 \\ 4 & 5 \end{bmatrix}, \tag{4}$$

where $\boldsymbol{B}$ is a matrix of size 6×2. Each element in the matrix $\boldsymbol{B}$ represents the row number of matrix $\boldsymbol{A}$. When filling the first row, the first three elements of the first row are obtained by randomly selecting any row of $\boldsymbol{A}$. The other elements of the first row are obtained by selecting from $\boldsymbol{A}$ and $\boldsymbol{B}$. More specifically, we randomly select a row from matrix $\boldsymbol{A}$ as the first three elements of the RCFA's first row and record the selected row number of matrix $\boldsymbol{A}$. We then choose an element from the same row number in matrix $\boldsymbol{B}$ to serve as the next three elements of RCFA's first row. Repeat this process for subsequent elements accordingly.

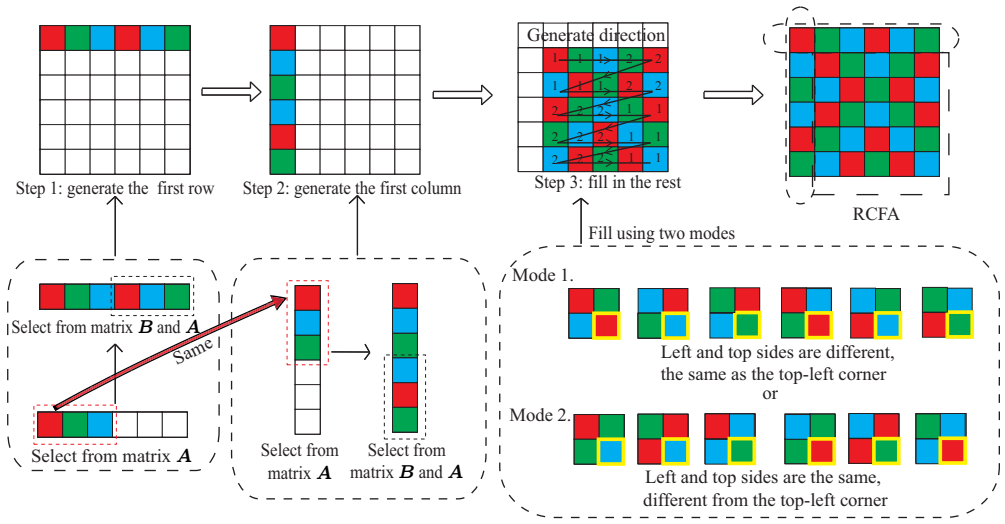


Fig. 2. RCFA generation algorithm.

Step 2 Generate the first column. The filling method for the first column is the same as that for the first row. However, it is important to note that the first element in the first column must be the same as the first element in the first row.

Step 3 Fill in the rest. Follow the generation direction of Fig. 2. Based on whether the colors on the left and top sides of the filling position are the same, choose between two filling modes. If different, select mode 1; if the same, select mode 2. Continue this process until the entire RCFA is filled.

Now, let us take Fig. 2 as an example to explain the algorithm in detail. First, perform Step 1. Select the first row of matrix $\boldsymbol{A}$ (denoted by $\boldsymbol{A}(1,:)$) to form the first three elements of the RCFA. Since $\boldsymbol{A}(1,:)$ was selected, the subsequent choice can only be made between $B(1,1)$ and $B(1,2)$. In Fig. 2, $B(1,1)$ is chosen to form the next three elements. Next, proceed to Step 2. Since $M(1,1)$ is R, for the first three elements in the first column, we can only choose either $\boldsymbol{A}(1,:)$ or $\boldsymbol{A}(2,:)$. In Fig. 2, $\boldsymbol{A}(2,:)$ is selected. The subsequent choice can only be made between $B(2,1)$ and $B(2,2)$, and then $B(2,2)$ is chosen for the next three. Finally, proceed to Step 3. First, fill $M(2,2)$. Since $M(2,1)$ and $M(1,2)$ have different colors, mode 1 is selected, and it is filled with R. Then, fill $M(2,3)$. Since $M(2,2)$ and $M(1,3)$ have different colors, mode 1 is selected again, and it is filled with G, continuing this process until the entire RCFA is filled.

The color Fourier pattern is now projected onto the object through a projector, and a single-pixel detector is used to collect various types of light in the scene. The total light intensity it collects can be expressed as

$$T_\phi(f_x, f_y) = \iint L_\phi(x, y; f_x, f_y) \times O(x, y)\,\mathrm{d}x\mathrm{d}y + T_n, \tag{5}$$

where T_ϕ represents the total light intensity when the Fourier pattern phase shift is ϕ, $O(x,y)$ represents the object, and T_n represents the ambient light. We now use three-step phase shifting to reconstruct the Fourier spectrum, which can be written as

$$\begin{aligned} \mathcal{F}\{O(x,y)\} = &\left[2T_0(f_x,f_y) - T_{\frac{2\pi}{3}}(f_x,f_y) - T_{\frac{3\pi}{4}}(f_x,f_y)\right] \\ &+ \sqrt{3}\mathrm{j}\left[T_{\frac{2\pi}{3}}(f_x,f_y) - T_{\frac{3\pi}{4}}(f_x,f_y)\right], \end{aligned} \tag{6}$$

where $\mathcal{F}\{\cdot\}$ denotes the Fourier transform and j represents the imaginary unit. We then perform the Fourier inverse operation to obtain the mosaic image, which can be expressed as

$$\begin{aligned} \widehat{O}(x,y) = \mathcal{F}^{-1}\Big\{ &\left[2T_0(f_x,f_y) - T_{\frac{2\pi}{3}}(f_x,f_y) - T_{\frac{3\pi}{4}}(f_x,f_y)\right] \\ &+ \sqrt{3}\mathrm{j}\left[T_{\frac{2\pi}{3}}(f_x,f_y) - T_{\frac{3\pi}{4}}(f_x,f_y)\right]\Big\}, \end{aligned} \tag{7}$$

where $\widehat{O}(x,y)$ represents the reconstructed image and $\mathcal{F}^{-1}\{\cdot\}$ represents the Fourier inverse operation.

Finally, in order to obtain the color image, we propose the RCFA-based demosaicing algorithm. Due to the structure of the RCFA, each pixel contains only one type of spectral information, while the other two types of spectral information need to be provided by a relevant algorithm. The steps of the algorithm are as follows:

Algorithm 1 RCFA-based demosaicing algorithm

Require: $\{(x, y, \widehat{O}(x, y))\}$, (x_q, y_q)

Ensure: z_q

Construct Voronoi diagram V from $\{(x, y, \widehat{O}(x, y))\}$

Reconstruct V' by including (x_q, y_q)

Identify intersected Voronoi polygons $V_i \in V$ with $V_q \in V'$

Define participant set $P = \{(x, y, \widehat{O}(x, y)) | V_i \text{ intersects } V_q\}$

for $(x, y, \widehat{O}(x, y)) \in P$ **do**

Compute area of intersection $A_i = \text{Area}(V_i \cap V_q)$

Compute total intersection area $A_{\text{total}} = \sum_{(x,y,\widehat{O}(x,y))\in P} \text{Area}(V_j \cap V_q)$

Compute normalized weight $w_i = \frac{A_i}{A_{\text{total}}}$

end for

Compute interpolated value

$$z_q = \sum_{(x,y,\widehat{O}(x,y))\in P} w_i \cdot z_i$$

return z_q

Here $(x, y, \widehat{O}(x, y))$ is obtained using Eq. (7); this states that the pixel value at position (x, y) is $\widehat{O}(x, y)$. (x_q, y_q) represents the unknown point, and z_q is the interpolation result. V is the Voronoi polygon formed by the known points, and V_i is one of its subsets. V' is the new Voronoi polygon formed after adding the unknown point, and V_q is one of its subsets. A_i is the intersection area between the old and new Voronoi polygons, A_{total} is the total intersection area, and w_i is the weight. To illustrate this algorithm more clearly, Fig. 3 is used as an example to further explain the algorithm.

As shown in Fig. 3, to obtain the pixel value of the red channel at a certain position, we first extract the red channel information from $(x, y, \widehat{O}(x, y))$, including the position information and pixel values. They are represented by z_i $(i = 1, 2, \ldots, 5)$ in Fig. 3. Then, based on z_i, a Voronoi polygon V (blue boundary polygon) is constructed. After adding an unknown point, a new Voronoi polygon V' (black boundary polygon) is constructed. Next, the intersection A_i (red boundary polygon) of V and V' is determined sequentially, and the area of each A_i is calculated. The total area sum is denoted by A_{total}. The weight is given by A_i/A_{total}, which represents the contribution of z_i to the final interpolated value z_q. Summing over i gives the final interpolated result. By the same token, to obtain the interpolation result for the green or blue channel at a certain position, first extract the green or blue channel information from $(x, y, \widehat{O}(x, y))$, and then follow the algorithm steps.

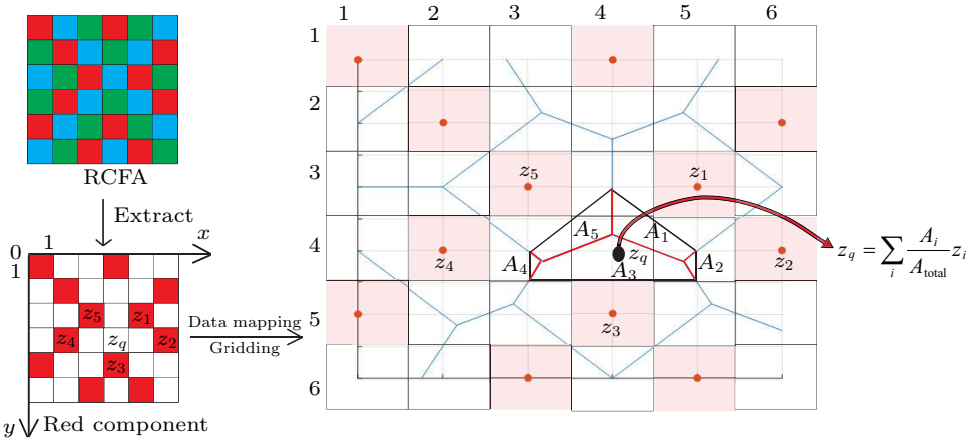


Fig. 3. RCFA-based demosaicing algorithm.

3. Results and analysis

3.1. Simulation results

In this section, the feasibility as well as the advantages of this scheme are verified by numerical simulation. In order to quantitatively evaluate the quality of the reconstructed image, the following MSE and PSNR are used:

$$\mathrm{MSE} = \frac{1}{N \times M \times 3} \sum_{i=1}^{N} \sum_{j=1}^{M} \sum_{k=1}^{3} \left(C(i,j,k) - O(i,j,k)\right)^2, \quad (8)$$

$$\mathrm{PSNR} = 20 \times \log_{10} \left(\frac{\max_{\mathrm{I}}}{\sqrt{\mathrm{MSE}}} \right) \mathrm{dB}, \quad (9)$$

where $N \times M$ is the size of the image, $O(i,j,k)$ denotes the pixel value on the original image position (i,j) used for simulation, $C(i,j,k)$ is the pixel value on the reconstructed image position (i,j), k stands for the three channels, i.e., RGB, respectively, and $\max_{\mathrm{I}}$ denotes the maximum pixel value in the image. Generally speaking, the smaller the MSE value and the larger the PSNR value, the higher the quality of the reconstructed image.

First of all, we verify the feasibility of the scheme. The simulation results are shown in Fig. 4.

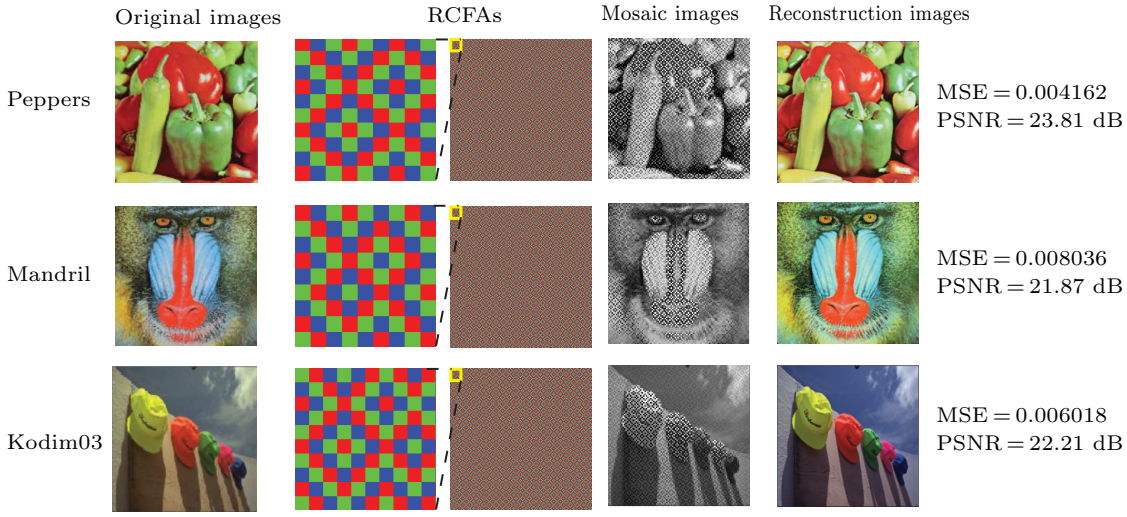


Fig. 4. Simulation results for the FSI-RCFA method.

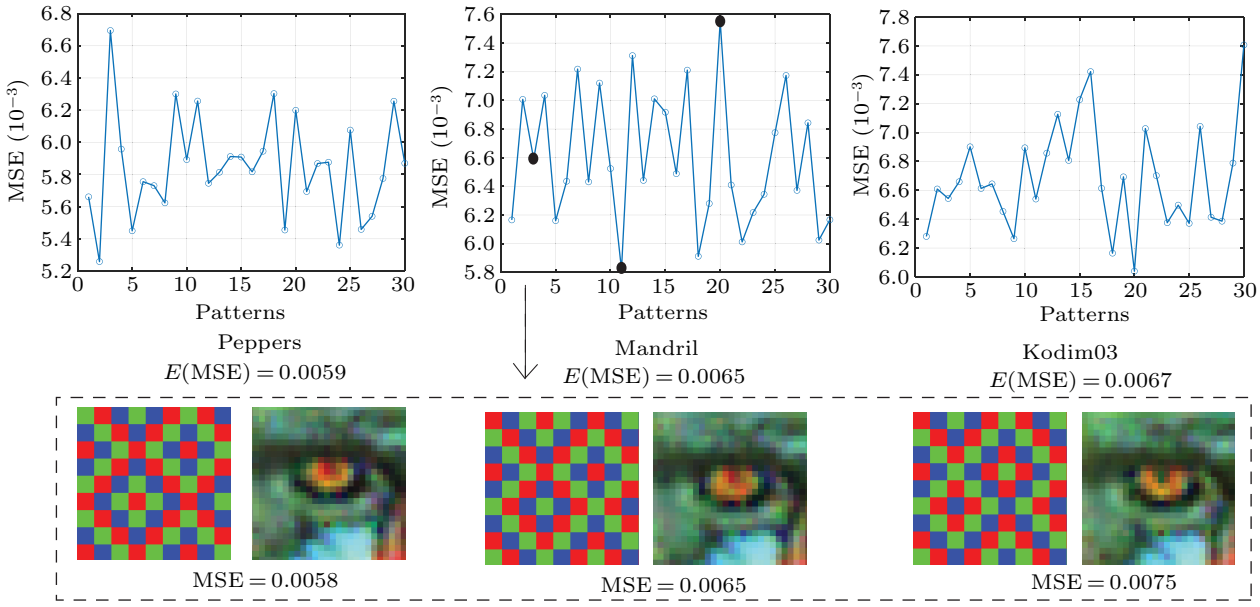


Fig. 5. The results of the FSI-RCFA method for different RCFA types (30 in total).

The reconstructed image has a pixel size of 255×255. After randomly generating an RCFA, the experiment is conducted according to the FSI-RCFA method, resulting in the mosaic image and the reconstructed image. The results show that for three images with different spectral characteristics, the reconstructed color images all have lower MSE values and higher PSNR values, confirming the feasibility of this scheme. Furthermore, the image quality varies for different RCFA types, as shown in Fig. 5.

The reconstructed image has a pixel size of 100×100, and $E(\mathrm{MSE})$ represents the expected value of the MSE. Figure 5 shows the curve of the MSE of the reconstructed images

as the RCFA type changes. It also displays the reconstruction details at the lowest MSE, the central value, and the highest MSE. From Fig. 5, it can be seen that due to the random nature of RCFA generation, the image quality varies for different RCFA types, but the image quality fluctuates within a good range.

Furthermore, we compared the experimental results obtained using the FSI-BCFA method with those obtained using the FSI-RCFA method while keeping the image size, Fourier spectrum reconstruction method, and the demosaicing process (linear interpolation) consistent. The results are shown in Fig. 6.

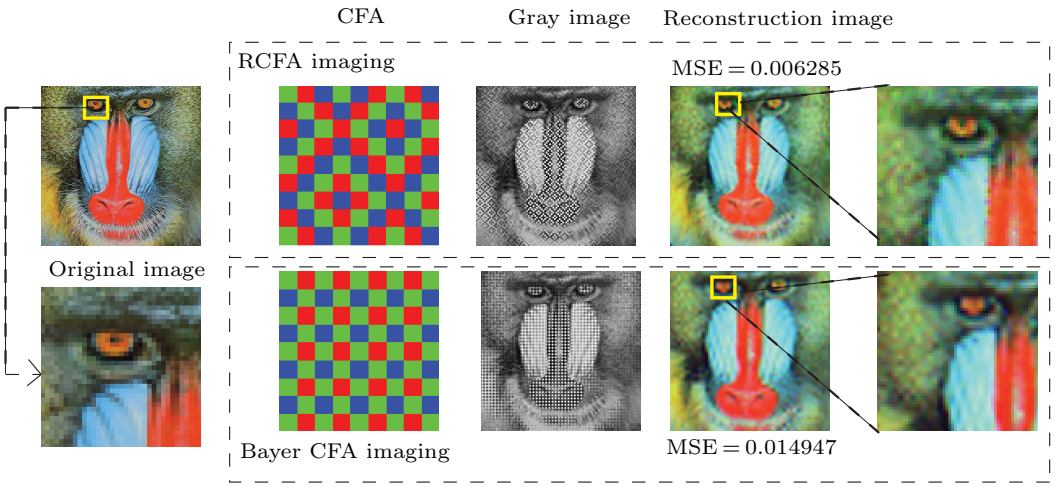


Fig. 6. Comparison between FSI-RCFA results and FSI-BCFA results.

Under the same experimental conditions, the experimental results obtained using the FSI-RCFA method have a lower MSE compared to those obtained using the FSI-BCFA method. When the BCFA method is used, the demosaicing quality tends to decrease in areas with high-frequency content. In contrast, the RCFA method ensures a more even distribution of chrominance energy in the frequency domain, thereby reducing the interference between chrominance and luminance signals, which improves the image quality. We then simulated each of the three images shown in Fig. 4 and calculated the respective MSEs using Eq. (8), as shown in Table 1.

Table 1. Imaging quality differences.

Method	Peppers	Mandril	Kodim03
FSI-RCFA	0.0059	0.0065	0.0067
FSI-BCFA	0.0149	0.0115	0.0092

The MSE for image reconstruction using RCFA in Table 1 is E(MSE). For different imaging subjects, the imaging quality of the RCFA scheme is superior to that of the BCFA scheme.

Next, we tested the noise resistance performance of the FSI-RCFA method and studied the variation of PSNR under Gaussian noise interference within a certain intensity range for two imaging schemes, as shown in Fig. 7. Analysis of Fig. 7 shows that under the same intensity of noise interference, the image quality of imaging obtained using the RCFA method is better than that obtained using the BCFA method, which also demonstrates the superior anti-noise performance of random CFA. In order to visualize the difference between the two in detail, we compare the differences between images reconstructed under three noise intensities, namely, 0.01, 0.03, and 0.05. From the experimental results, it can be seen that the images reconstructed using the RCFA method have clearer eye contours compared to those reconstructed using the BCFA method under different levels of noise interference.

Finally, we analyze the advantages of the RCFA method for specific scenarios. The RCFA generation algorithm can produce RCFAs with different spatial structures, greatly increasing design flexibility compared to the fixed-position BCFA. For instance, when obtaining single-channel pixel values at specific locations in an image, RCFA has a significant advantage. This is particularly evident in the domain of vegetable production: by comparing the variation in pixel values across different color channels (such as red and green channels), it is possible to identify lesions on leaves or fruits. However, these lesions may not necessarily exhibit periodic spatial characteristics. When imaging is performed using the BCFA method, it is necessary to use adjacent information at the location to interpolate and obtain the missing color components, which may result in varying degrees of error. In contrast, the RCFA method allows for spatial structure design based on specific needs, enabling more accurate single-channel pixel values without increasing the number of measurements. Taking the example of a specific demand for the red channel pixel values at the five locations identified in the lower right corner when reconstructing the image, the data pairs obtained using the two methods are as shown in Fig. 8. Let us design the corresponding RCFA based on the requirements and extract the

appropriate data. We use the following formula to calculate the error:

$$\text{Error} = \frac{1}{N}\sum_i\sum_j |C(i,j) - O(i,j)|, \tag{10}$$

where $O(i,j)$ denotes the single-channel pixel value at a specific location (i,j) in the original image, and $C(i,j)$ is the single-channel pixel value at the corresponding location (i,j) in the reconstructed image. N is the total number of pixel points selected. According to the experimental results shown in Fig. 8, the red channel pixel values obtained at specific locations using the RCFA method are more accurate. This is because these values were obtained from direct measurements and have not been interpolated for estimation. Of course, accurate values at these discrete locations can also be obtained using the BCFA method, but this requires a combination of multiple Bayer modes, which undoubtedly increases the number of measurements, whereas the RCFA result can be obtained from only one measurement. Therefore, due to the flexibility in the design of the stochastic CFA, it is more advantageous than the fixed-position periodic CFA in some specific scenarios.

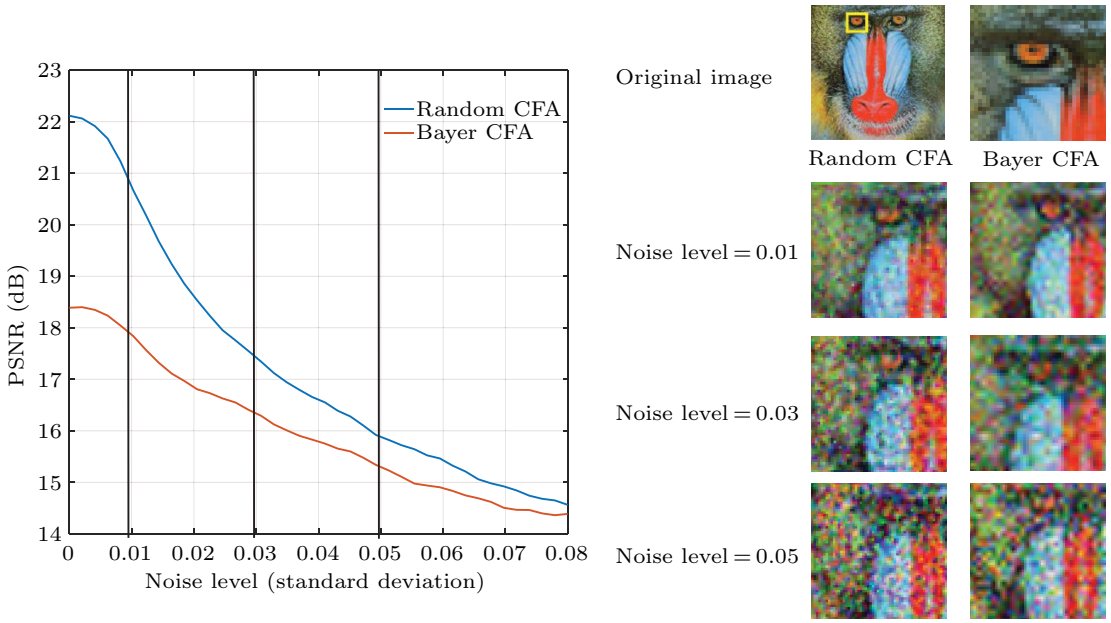


Fig. 7. Noise immunity performance analysis.

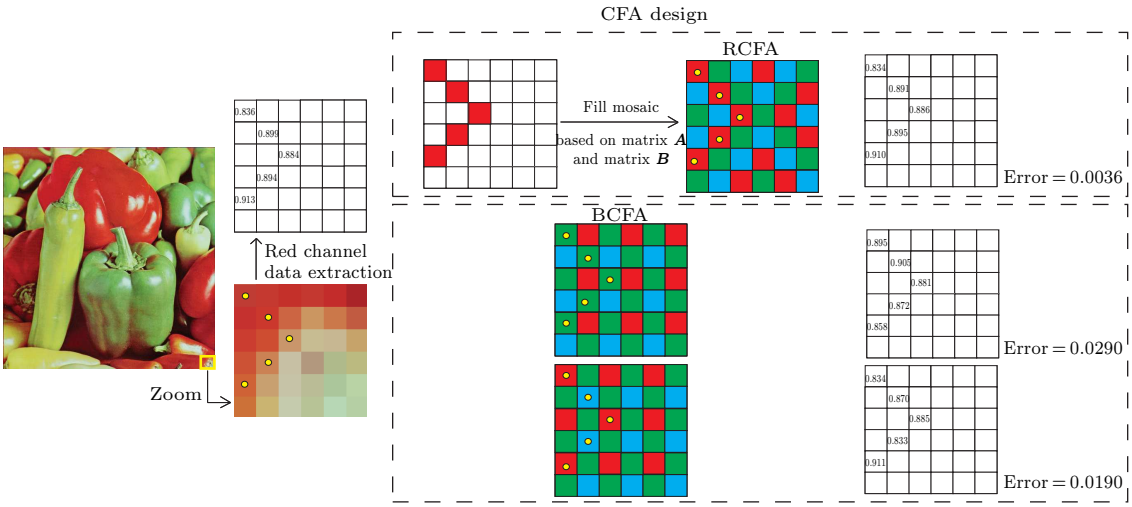


Fig. 8. Differences in the reconstruction of single-channel pixel values at specific locations.

3.2. Experimental results

We verified the proposed scheme through experiments. Figure 9 shows the experimental setup. In the experiment, toy dolls were used as test objects. Three groups of RGB LED light sources were projected in a time-division manner and modulated by a digital micromirror device (DMD, ViALUX V-7001) to generate color-based patterns. These patterns were transmitted through the projection lens and then projected onto the doll. Subsequently, the light reflected by the object was

collected by a photodetector (Thorlabs PMM02), and the measured data was converted by an analog-to-digital converter (NI USB-6341) before being transmitted to the PC. At the PC, a color image was reconstructed by applying the corresponding demosaicing algorithm.

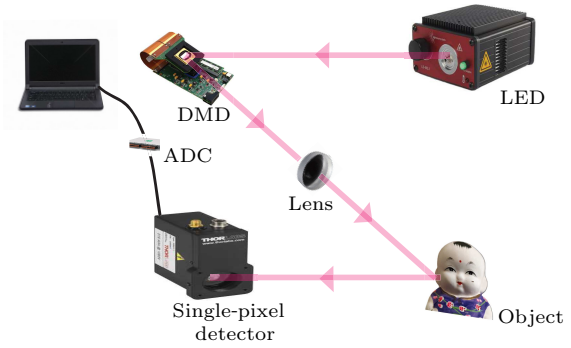


Fig. 9. Experimental setup.

In the experiment, three groups of LED light sources (RGB) were projected in a time-division manner. Two types of color mask templates were loaded via the DMD: the FSI-BCFA group used the BCFA method, while the FSI-RCFA group employed the RCFA method (generated according to the algorithm in Section 2). After the data was collected by the PC, the FSI-BCFA group was processed using traditional bilinear interpolation, whereas the FSI-RCFA group was processed using the RCFA-based demosaicing algorithm. All reconstructed images were sized at 50×50. The experimental results are shown in Fig. 10.

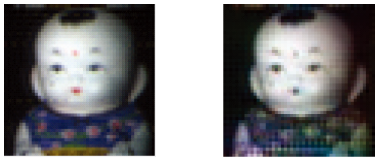


Fig. 10. Comparison of experimental results.

The experimental results indicate that the FSI-RCFA method significantly outperforms the FSI-BCFA method in terms of the subjective visual quality of the reconstructed images. Specifically, details such as the facial textures and clothing wrinkles of the doll are clearer in the FSI-RCFA reconstructed images, and the color reproduction is closer to the real object. In contrast, the FSI-BCFA reconstructed images exhibit obvious artifacts and color aliasing, particularly in high-frequency texture regions. This outcome not only validates the feasibility of the FSI-RCFA method but also demonstrates that this scheme achieves higher imaging quality than the FSI-BCFA method.

4. Discussion

4.1. Theoretical analysis of the RCFA method

In this section, we will further discuss the design principles and advantages of the RCFA method from the perspective of theoretical analysis. To avoid spectral aliasing between luminance and chrominance and to facilitate subsequent processing, we consider standard orthogonal bases corresponding to luminance and chrominance components, which are defined as[32]

$$\begin{cases} \boldsymbol{L} = \frac{1}{\sqrt{3}}[1,1,1]^{\mathrm{T}}, \\ \boldsymbol{C}_1 = \frac{1}{\sqrt{2}}[-1,1,0]^{\mathrm{T}}, \\ \boldsymbol{C}_2 = \frac{1}{\sqrt{6}}[-1,-1,2]^{\mathrm{T}}, \end{cases} \tag{11}$$

where $\boldsymbol{L}$ represents the luminance component, which is a weighted average of R, G, and B, reflecting overall brightness. $\boldsymbol{C}_1$ represents the red–green chrominance difference, with coefficients of ± 1 for R and G to emphasize red–green contrast, while the coefficient for B is 0, as humans are more sensitive to red–green differences. A normalization factor of $1/\sqrt{2}$ ensures that $\|\boldsymbol{C}_1\| = 1$. For $\boldsymbol{C}_2$, the coefficients are -1 for both R and G, and 2 for B, capturing the blue–yellow contrast (the difference between B and R+G). A normalization factor of $1/\sqrt{6}$ ensures that $\|\boldsymbol{C}_2\| = 1$. By mapping the CFA color values to this orthogonal basis, the luminance and chrominance signals can be separated.

Then, to better quantify the spectral characteristics of the luminance and chrominance components, their power spectral density (PSD) functions need to be computed. We encode R, G, and B as follows: $\boldsymbol{R} = [1 \quad 0 \quad 0]^{\mathrm{T}}$, $\boldsymbol{G} = [0 \quad 1 \quad 0]^{\mathrm{T}}$, and $\boldsymbol{B} = [0 \quad 0 \quad 1]^{\mathrm{T}}$. For ease of computation, we construct a 3×3 basis matrix $\boldsymbol{V}$ based on Eq. (11):

$$\boldsymbol{V} = [\boldsymbol{L} \ \boldsymbol{C}_1 \ \boldsymbol{C}_2] = \begin{bmatrix} \frac{1}{\sqrt{3}} & -\frac{1}{\sqrt{2}} & -\frac{1}{\sqrt{6}} \\ \frac{1}{\sqrt{3}} & \frac{1}{\sqrt{2}} & -\frac{1}{\sqrt{6}} \\ \frac{1}{\sqrt{3}} & 0 & \frac{2}{\sqrt{6}} \end{bmatrix}. \tag{12}$$

For any pixel (x, y) in the CFA, its color is encoded as $\mathrm{cfa}(x,y) \in \{\boldsymbol{R}, \boldsymbol{G}, \boldsymbol{B}\}$. Using the basis matrix $\boldsymbol{V}$, the color at (x, y) can be mapped to the luminance–chrominance space

$$\begin{bmatrix} \boldsymbol{L}(x,y) \\ \boldsymbol{C}_1(x,y) \\ \boldsymbol{C}_2(x,y) \end{bmatrix} = \boldsymbol{V}^{\mathrm{T}} \cdot \mathrm{cfa}(x,y). \tag{13}$$

Taking a red pixel as an example, the mapping process is as follows:

$$\boldsymbol{V}^{\mathrm{T}} \cdot \boldsymbol{R} = \begin{bmatrix} \frac{1}{\sqrt{3}} & \frac{1}{\sqrt{3}} & \frac{1}{\sqrt{3}} \\ -\frac{1}{\sqrt{2}} & \frac{1}{\sqrt{2}} & 0 \\ -\frac{1}{\sqrt{6}} & -\frac{1}{\sqrt{6}} & \frac{2}{\sqrt{6}} \end{bmatrix} \begin{bmatrix} 1 \\ 0 \\ 0 \end{bmatrix} = \begin{bmatrix} \frac{1}{\sqrt{3}} \\ -\frac{1}{\sqrt{2}} \\ -\frac{1}{\sqrt{6}} \end{bmatrix}. \tag{14}$$

By iterating over all pixel positions (x, y), the luminance matrix $\boldsymbol{L}(x,y)$ and the chrominance matrices $\boldsymbol{C}_1(x,y)$, $\boldsymbol{C}_2(x,y)$ of the CFA can be obtained. Next, the 2D DFT is applied to the luminance and chrominance matrices:

$$\mathcal{F}\{\boldsymbol{U}_k\}(\omega_x, \omega_y) = \sum_{x=0}^{N_x-1} \sum_{y=0}^{N_y-1} \boldsymbol{U}_k(x,y)\, \mathrm{e}^{-\mathrm{j}(\omega_x x + \omega_y y)}, \tag{15}$$

$$\boldsymbol{U}_k(x,y)\begin{cases}\boldsymbol{L}(x,y), & k=1,\\ \boldsymbol{C}_1(x,y), & k=2,\\ \boldsymbol{C}_2(x,y), & k=3,\end{cases} \tag{16}$$

where N_x and N_y represent the sizes of $\boldsymbol{U}_k(x,y)$ in the x and y directions, respectively. ω_x and ω_y represent the angular frequencies in the x and y directions. Then, the square of the magnitude of the Fourier transform is taken and normalized, yielding the expression for the PSD

$$\mathrm{PSD}(\omega_x,\omega_y)=\frac{\left|\mathcal{F}\{\boldsymbol{U}_k\}(\omega_x,\omega_y)\right|^2}{N_xN_y}. \tag{17}$$

To analyze the spectral distribution of the chrominance components, we define the low-frequency region ($\|\omega\|<2\pi/3$) and the high-frequency region ($\|\omega\|\geq 2\pi/3$), where $\|\omega\|=\sqrt{\omega_x^2+\omega_y^2}$. The low-frequency energy ratio is calculated using

$$\eta=\frac{\sum_{\|\omega\|<\frac{2\pi}{3}}\mathrm{PSD}(\omega)}{\sum_{\|\omega\|}\mathrm{PSD}(\omega)}\times 100\%, \tag{18}$$

while the high-frequency energy ratio is $1-\eta$. The results obtained by calculating the PSD energy distribution for the RCFA method and the BCFA method are shown in Tables 2 and 3.

Table 2. Luminance energy distributions obtained using the RCFA and BCFA methods.

Method	Low frequency (%)	High frequency (%)
RCFA	100	0
BCFA	100	0

Table 3. Chrominance energy distributions obtained using the RCFA and BCFA methods.

Method	Low frequency (%)	High frequency (%)
RCFA	4.7 ± 0.3	95.3 ± 0.3
BCFA	8.3	91.7

To obtain the results shown in Tables 2 and 3, the BCFA and RCFA methods were applied to the same image size of 100×100. Table 2 demonstrates the inherent sparsity of natural images, as evidenced by the fact that most of the energy in the Fourier domain of the luminance component is concentrated in the low-frequency region.

For Table 3, due to the inherent randomness in the spatial structure of the RCFA, its energy distribution exhibits fluctuations of around 0.3%. In the design of the RCFA, high-frequency oscillations are introduced in the spatial domain by enforcing color differences between adjacent pixels. This causes the PSD energy of the chrominance components to concentrate in the high-frequency region, thereby improving the separation from the low-frequency luminance components and reducing aliasing between the two.

4.2. Comparison of mosaic decoding algorithms

In this section, we will compare the RCFA-based demosaicing algorithm proposed in Section 2 with other widely used demosaicing algorithms, such as bilinear interpolation and gradient-adaptive interpolation, and analyze the differences between them as well as the advantages of our algorithm.

First, let us briefly introduce these two algorithms. The bilinear interpolation algorithm is a classic interpolation method based on grid data in two-dimensional space. Its core idea is to combine two one-dimensional linear interpolations in the horizontal and vertical directions, which can ultimately be represented as a weighted average of the four vertices, with weights that are related to the distance to the sample points.[34] On the other hand, the core idea of the gradient-adaptive algorithm is to dynamically adjust the interpolation path by analyzing the gradient direction in the local region of the image. This allows us to preferentially reconstruct colors along the edge directions, thus reducing artifacts caused by cross-edge interpolation.[35] We now apply the above methods to the FSI-RCFA scheme and use Fourier single-pixel imaging with a Bayer color filter array (FSI-BCFA) as a comparison. The reconstruction results are shown in Fig. 11.

From the results, the RCFA-based demosaicing algorithm clearly outperforms the two widely used methods. The fundamental reason lies in the fact that an RCFA, unlike a periodic CFA, exhibits strong spatial randomness. The RCFA-based algorithm approaches the problem from this perspective, performing interpolation and reconstruction by dynamically constructing the geometric distribution and area weights of the color channels. It is highly suited for irregular sampling. For BCFA, which involves regular sampling, the algorithm also demonstrates a certain degree of adaptability.

For bilinear interpolation, due to the periodic structure of the BCFA, the neighborhood color distribution is predictable, and interpolation weights can be calculated using a fixed template. However, the random distribution of the RCFA leads to irregular sampling, where sparse and irregular neighboring sampling points cause the distance-weighted model to fail, resulting in interpolation that relies on a few random neighboring points.

For gradient-adaptive interpolation, the periodicity of the BCFA allows for the decoupling of gradient calculation from the color channels, ensuring reliable gradient directions and effective interpolation path optimization. In contrast, the non-periodic structure of the RCFA disrupts the reliability of gradient directions, leading to misjudgments of interpolation paths and high-frequency chromatic energy leakage, significantly degrading the reconstruction quality. This highlights the inherent contradiction between the two traditional demosaicing algorithms and the random sampling system.

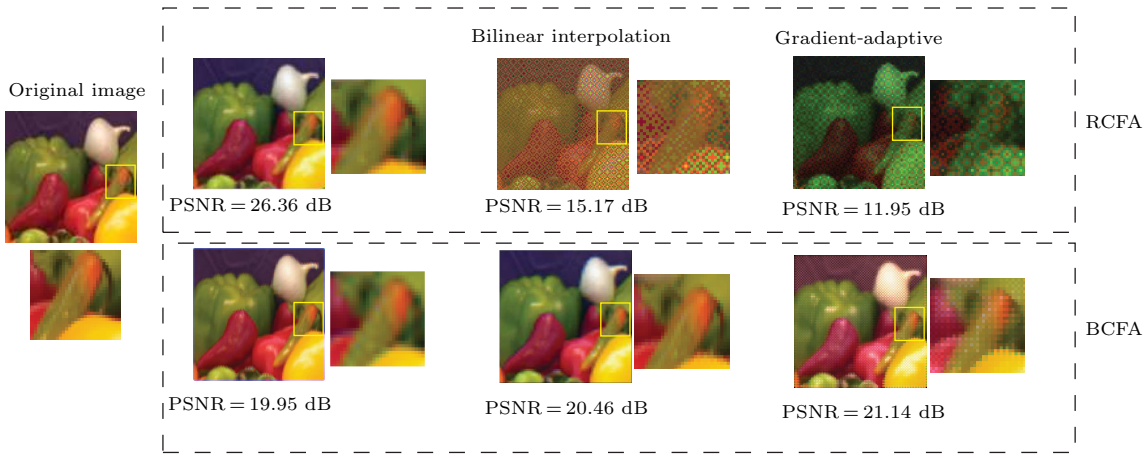


Fig. 11. Comparison of images reconstructed using different demosaicing algorithms.

5. Conclusion

We propose the FSI-RCFA method to address spectral aliasing in color imaging. By integrating RCFA modulation with an RCFA-based demosaicing algorithm, our method achieves superior separation of chrominance and luminance in the frequency domain. Numerical simulation results demonstrate that the FSI-RCFA method has advantages over the FSI-BCFA method. The MSE is effectively suppressed, and the noise resilience is significantly improved. We can utilize the RCFA generation algorithm to minimize interpolation errors in targeted scenarios, enabling precise single-channel pixel measurements for applications such as agricultural defect detection. Future directions will focus on real-time algorithm optimization and hybrid CFA designs to enhance dynamic imaging and multispectral applications.

Acknowledgement

This project was supported by the National Natural Science Foundation of China (Grant Nos. 62001249 and 62375140).

References

[1] Gatti A, Brambilla E, Bache M and Lugiato L A 2004 *Phys. Rev. Lett.* **93** 093602
[2] Sun B Q, Welsh S S, Edgar M P, Shapiro J H and Padgett M J 2012 *Opt. Express* **20** 16892
[3] Li H G, Zhang D J, Xu D Q, Zhao Q L, Wang S, Wang H B, Xiong J and Wang K 2015 *Phys. Rev. A* **92** 043816
[4] Welsh S S, Edgar M P, Bowman R, Jonathan P, Sun B Q and Padgett M J 2013 *Opt. Express* **21** 23068
[5] Nakano A 2002 *Cell Struct. Funct.* **27** 349
[6] Pittman T B, Shih Y H, Strekalov D V and Sergienko A V 1995 *Phys. Rev. A* **52** R3429
[7] Bennink R S, Bentley S J and Boyd R W 2002 *Phys. Rev. Lett.* **89** 113601
[8] Katz O, Bromberg Y and Silberberg Y 2009 *Appl. Phys. Lett.* **95** 131101
[9] Bie S H, Wang C H, Lv R B, Bao Q Q, Fu Q, Meng S Y and Chen X H 2023 *Chin. Phys. B* **32** 128702
[10] Zhao Y N, Hou H Y, Han J C, Cao D Z, Zhang S H, Liu H C and Liang B L 2023 *Chin. Phys. B* **32** 064201
[11] Zhang Z B, Wang X Y, Zheng G A and Zhong J G 2017 *Opt. Express* **25** 19619
[12] Liu Z D, Zhang X Q, Ding Y N, Li Z G and Li H G 2025 *Opt. Express* **33** 5684
[13] Wang Z H, Wen Y A, Ma Y, Tian Y L, Cui Y Z, Peng W, Wang F F and Lu Y 2024 *Opt. Express* **32** 41255
[14] Wang L and Zhao S M 2016 *Photon. Res.* **4** 240
[15] Xu Z H, Chen W, Penuelas J, Padgett M and Sun M J 2018 *Opt. Express* **26** 2427
[16] Shao H, Huang H, Wei Y X, Zhang H J, Yang Z H and Yu Y J 2024 *Chin. Phys. Lett.* **41** 124202
[17] Radwell N, Mitchell K J, Gibson G M, Edgar M P, Bowman R and Padgett M J 2014 *Optica* **1** 285
[18] Wang Y W, Suo J L, Fan J T and Dai Q H 2015 *IEEE Photon. Technol. Lett.* **28** 288
[19] Zhao Y N, Hou H Y, Han J C, Liu H C, Zhang S H, Cao D Z and Liang B L 2021 *Opt. Lett.* **46** 4900
[20] Ji P C, Wu Q F, Shi Y Y, Yang Z H and Yu Y J 2024 *Opt. Express* **32** 45635
[21] Wang L and Zhao S M 2021 *Opt. Express* **29** 24486
[22] Cao D Z, Xu B L, Zhang S H and Wang K G 2015 *Chin. Phys. Lett.* **32** 114208
[23] Duan D Y, Zhu R and Xia Y J 2021 *Opt. Lett.* **46** 4172
[24] Wei Y, Shi Y Y, Zhang M L, Zhang D J and Liu Y W 2025 *Opt. Laser Technol.* **181** 111875
[25] Jiang X Y, Li Z W, Du G, Jia J L, Wang Q H, Chi N and Dai Q H 2022 *Opt. Express* **30** 25995
[26] Sun Y S, Jian H, Shi D F, Zha L B, Guo Z J, Yuan K, Hu S X and Wang Y J 2022 *Opt. Express* **30** 31728
[27] Xie J T, Tan J H, Bie S H, Li M F, Chen L M and Wu L A 2024 *Opt. Lett.* **49** 4162
[28] Li T X, Chen Y, Wang H, Liu S, Zhang L and Li Z 2019 *Opt. Express* **27** 23138
[29] Zhang Z B, Wang X, Zheng G B, Li D H and Zhai G J 2017 *Sci. Rep.* **7** 12029
[30] Zhang Z B, Liu S L, Peng J Z, Yao M H, Zheng G A and Zhong J G 2018 *Optica* **5** 315
[31] Bayer B 1976 U.S. Patent 3971065 [1976]
[32] Condat L 2009 *Proc. 16th IEEE International Conference on Image Processing (ICIP)*, November 7–10, 2009, Cairo, Egypt, p. 1625
[33] Sibson R 1981 *A Brief Description of Natural Neighbour Interpolation in Interpreting Multivariate Data*, p. 21
[34] Gunturk B K, Glotzbach J, Altunbasak Y, Schafer R W and Mersereau R M 2005 *IEEE Signal Processing Magazine* **22** p. 44
[35] Malvar H S, He L W and Cutler R 2004 *Proceedings of the* 2004 *IEEE International Conference on Acoustics, Speech, and Signal Processing (IEEE)* **3** p. 485